Direct and Gradient-Based Average Strain Estimation by Using Weighted Nearest Neighbor Cross-Correlation Peaks

Mohammad Arafat Hussain, Emran Mohammad Abu Anas, S. Kaisar Alam, *Senior Member, IEEE*, Soo Yeol Lee, and Md. Kamrul Hasan, *Senior Member, IEEE*

Abstract—In this paper, two novel approaches, gradient-based and direct strain estimation techniques, are proposed for high-quality average strain imaging incorporating a cost function maximization. Stiffness typically is a continuous function. Consequently, stiffness of proximal tissues is very close to that of the tissue corresponding to a given data window. Hence, a cost function is defined from exponentially weighted neighboring pre- and post-compression RF echo normalized cross-correlation peaks in the lateral (for displacement estimation) or in both the axial and the lateral (for direct strain estimation) directions. This enforces a controlled continuity in displacement/strain and average displacement/strain is calculated from the corresponding maximized cost function. Axial stress causes lateral shift in the tissue. Therefore, a 1-D post-compression echo segment is selected by incorporating Poisson's ratio. Two stretching factors are considered simultaneously in gradient-based strain estimation that allow imaging the lesions properly. The proposed time-domain gradient-based and direct-strain-estimation-based algorithms demonstrate significantly better performance in terms of elastographic signal-to-noise ratio (SNRe), elastographic contrast-to-noise ratio (CNRe), peak signal-to-noise ratio (PSNR), and mean structural similarity (MSSIM) than the other reported time-domain gradient-based and direct-strain-estimation techniques in finite element modeling (FEM) simulation and phantom experiments. For example, in FEM simulation, it has been found that the proposed direct strain estimation method can improve up to approximately 2.49 to 8.71, 2.2 to 6.63, 1.5 to 5, and 1.59 to 2.45 dB in the SNRe, CNRe, PSNR, and MSSIM compared with the traditional direct strain estimation method, respectively, and the proposed gradient-based algorithm demonstrates 2.99 to 16.26, 18.74 to 23.88, 3 to 9.5, and 0.6 to 5.36 dB improvement in the SNRe, CNRe, PSNR, and MSSIM, respectively, compared with a recently reported time-domain gradient-based technique. The range of improvement as noted above is for low to high applied strains. In addition, the comparative results using the *in vivo* breast data (including malignant or benign masses) also show that the lesion size is better defined by the proposed gradient-based average strain estimation technique.

I. Introduction

VISUALIZATION of discriminant elastic properties in the art of pathological diagnosis of tissue abnormality is performed in the form of elastography. In quasi-static elasticity imaging, ultrasound echoes are acquired before and after applying gentle external pressure on the surface, typically by means of an ultrasound transducer. Different algorithms are developed to calculate strain from these pre- and post-compression echoes. These strain-estimation algorithms can be broadly categorized into 1) gradient-based strain estimation [1]–[6], and 2) direct strain estimation [7]–[10]. In most cases, gradient-based techniques are developed with a target of real-time imaging whereas direct strain estimation techniques focus on the development of high-quality strain image at the cost of increased computational complexity. However, RF echo decorrelation and noise degrade the performance of the algorithms for both categories.

The gradient-based strain estimation relies on calculating displacement from the cross-correlation between pre- and post-compression RF windowed echo segments. It always introduces a significant amount of noise in the strain due to small window selection and/or large overlap between the successive choice of windows of the same echo line [7]. According to [11], equal or greater than 90% overlap between successive windows can generate strain image of high axial resolution, but also introduces noise in the form of worm artifacts [8]. High-frequency noise is generally amplified by the gradient-based techniques [6], [9]. Temporal stretching of post-compression echo improves the cross-correlation between pre- and post-compression signals by minimizing the strain noise [3], but it is effective only in low strain [12] and has a high probability of missing hard lesions. Before gradient operation, a smoothing technique based on least-squares-based linear regression [13] or least-squared-error-based smoothing-spline [6] can be applied on the displacement matrix. Median filtering is also effective before gradient operation to remove the shot noise and some false peak noise. For smoothing the strain image, some recent literature [5], [14]–[16] proposes to consider the previous windows or sample characteristic values in computing the present displacement value to maintain continuity of strain. But these smoothing algorithms are not intelligent enough to detect and preserve the lesion edge.

In direct strain estimation, the strain is directly calculated from a pair of pre- and post-compression RF-echo segments in the time domain [7] or frequency domain [9], [10]. The adaptive stretching-based direct strain estimation is better in the time domain than in the frequency domain. Direct spectral strain estimation is a non-coherent technique because it ignores the signal phase. But it is robust on the undesired scanning motion from an unstable handheld probe and undesired internal tissue motion [17]. It is considered that the post-compression echo is a compressed and delayed version of its counterpart precompression echo [7]. This signal model inspires the idea of stretching the post-compression echo or shifting the pre-compression signal spectrum before the cross-correlation calculation. These techniques can generate a strain image with higher SNR than gradient-based techniques, but the elastogram produced by the direct strain estimation techniques has no strain continuity guarantee among neighboring pixels of a particular area of the strain image.

In this paper, we propose two novel techniques for strain estimation: 1) the direct average strain estimation (DASE), and 2) the gradient-based average strain estimation (GBASE). In both techniques, regularization of strain continuity is ensured without using any prior estimates of the displacement or strain; both make use of a cost function to apply exponential weights to normalized cross-correlation (NCC) peaks in the lateral (for GBASE) or in both the lateral and the axial (for DASE) directions. Because of the similarity of the physical properties of the neighboring tissue elements, it is assumed that the strain at a particular point has similarity with its neighbor in both the axial and the lateral directions whereas displacement at a particular point is almost coherent with its neighbor in the lateral direction. The average displacement or strain value is calculated from the corresponding cost function defined for each of the pixels. The exponential weight attached with the cost function ensures less distortion at the lesion boundary. The performance of this algorithm is evaluated using a finite-element modeling (FEM) phantom and experimental phantom as well as *in vivo* data and compared with other recently reported gradient-based and direct strain estimation algorithms.

The paper is organized as follows. Section II describes the proposed direct and gradient-based strain estimation techniques. Section III presents the simulation and experimental results to demonstrate the strength of the algorithms. Concluding remarks are presented in Section IV.

II. Methods

A. The Signal Model

Symbols and acronyms used in this paper are presented in Table I.

The simplified 1-D model of the backscattered ultrasound RF signals before and after compression are given by [7]:

$$r_1(t) = s_1(t) + v_1(t) = s(t) * p(t) + v_1(t), \quad (1)$$

$$r_2(t) = s_2(t) + v_2(t) = s\left(\frac{t}{a} - t_0\right) * p(t) + v_2(t), \quad (2)$$

TABLE I. Symbols and Acronyms.

| Symbols	Definitions
L_v	Inter-window shift between two consecutive radio-frequency echo segments
L_i	Length of radio-frequency echo segments
L_w	Width of 2-D windowed radio-frequency echo segment
N_c	Number of scan lines in a single ultrasound image
s_{avg}	Applied strain
ν	Poisson's ratio
$\{L_a, L_l\}$	Nearest neighbor factors in the axial and lateral directions, respectively
$\{\chi_a, \chi_l\}$	Weighting factors of the exponential weight function in the axial and lateral directions, respectively
AM	Analytic minimization
AS	Adaptive-stretching strain estimator
NCC	Normalized cross-correlation
CNRe	Elastographic contrast-to-noise ratio
DASE	Direct average strain estimation
FEM	Finite element modeling
GBASE	Gradient-based average strain estimation
MSE	Mean square error
SSIM	Structural similarity
MSSIM	Mean structural similarity
NN	Nearest neighbor
PSF	Point spread function
PSNR	Peak signal-to-noise ratio
RF	Radio-frequency
NSAD	Normalized sum of absolute differences
SNR	Signal-to-noise ratio
SNRe	Elastographic signal-to-noise ratio
NSSD	Normalized sum of squared differences
TGC	Time-gain-control
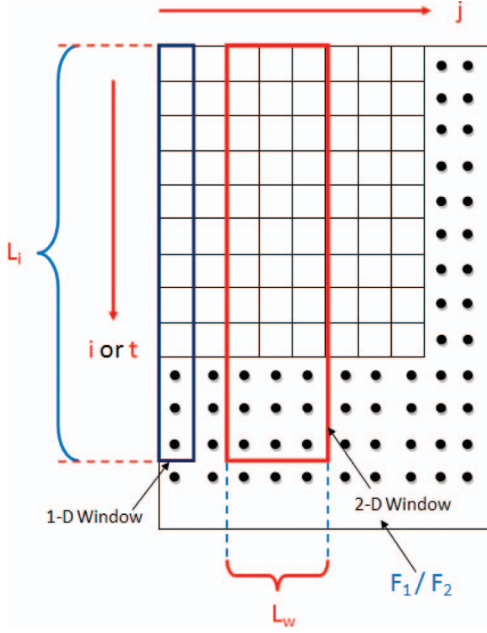
Fig. 1. 1-D and 2-D window selection from RF echo frame for 1-D DASE and 2-D DASE, respectively. Here, L_i is the axial length of the RF window (for both, the 1-D DASE and 2-D DASE methods) and L_w is the number of A-lines in the 2-D RF window (for the 2-D DASE method).

where $r_1(t)$ and $r_2(t)$ are the pre- and post-compression RF echo signals, respectively; $s(t)$ is the 1-D ultrasound scattering function; $p(t)$ denotes the point spread function (PSF) or ultrasound system response; a denotes the compression factor caused by mechanical deforming pressure to the medium; $v_1(t)$ and $v_2(t)$ are the uncorrelated random noise profiles; and * is used to denote the convolution operation. It is to be noted that this model assumes no out-of-plane motion upon compression, and in addition, the post-compression RF echo is assumed to be the scaled and shifted replica of the pre-compression RF echo in the absence of noise. According to [18], the strain s is related to the compression factor $1/a$ as $s = 1 - a$, where $a \leq 1$ and $s << 1$. Now the post-compression signal is stretched by a factor δ, i.e., $r_\delta(t) = r_2(\delta t)$. By neglecting the noise term [i.e., $v_\delta(t) = 0$], the NCC peak $\zeta_\delta(\tau)$ (≤ 1) can be defined as [12], [19],

$$\zeta_\delta(\tau) = \frac{\int_{-\infty}^{\infty} r_1(t) r_\delta(t + \tau) \mathrm{d}t}{\sqrt{\int_{-\infty}^{\infty} r_1^2(t) \int_{-\infty}^{\infty} r_\delta^2(t) \mathrm{d}t}}. \tag{3}$$

Eq. (3) becomes maximum for $\delta = a$ with the assumption of $p(\delta t) \cong p(t)$. Then the effective strain can be directly calculated from the stretching factor $\mathrm{s} = 1 - \delta_o$, where

$$\delta_o = \arg \max_\delta \{\zeta_\delta(\tau)\}. \tag{4}$$

B. Average Strain Estimation Using the Weighted Nearest Neighbor Method

To reduce the signal de-correlation that results from non-axial motion and introduce a built-in smoothing fea-

ture, we propose the DASE using the weighted nearest neighbor method. Due to the similarity of the physical properties of the tissue with its surroundings, calculated strain from a pair of windowed RF segments for a particular tissue point is assumed to be close to the strains in the neighboring tissues. This assumption is valid unless there is a sharp change in the tissue stiffness. To make the algorithm intelligent enough to cope with the situation, our proposed method incorporates an exponentially decaying weight that allows the tracking of a sharp change in the strain on the lesion boundary (discussed in the next section).

1) 1-Dimensional Direct Average Strain Estimation: Let $F_1(i, j)$ and $F_2(i, j)$ denote the pre- and post-compression ultrasound RF frames, respectively. Here, i denotes the axial depth index and j denotes the scan line or RF A-line indices (Fig. 1). To calculate the effective strain at a point (i_s, j_s) of the strain image, a corresponding pair of 1-D windowed RF segments $r_1^{(i_s,j_s)}$ and $r_2^{(i_s,j_s)}$ are selected from the pre- and post-compression ultrasound image frames as

$$r_1^{(i_s,j_s)}(i) = F_1((i_s - 1)L_v + i, j)$$
$$\text{for } 1 \leq i \leq L_i \text{ and } j = j_s, \text{ and} \tag{5}$$

$$r_2^{(i_s,j_s)}(i) = F_2(\text{round}((i_s - 1)(1 - s_{avg})L_v) + i, j)$$
$$\text{for } 1 \leq i \leq L_i \text{ and } j = j_s + \left(j_s - \frac{N_c}{2}\right) s_{avg} \nu, \tag{6}$$

where ν is Poisson's ratio, s_{avg} is the approximate applied strain, N_c is the number of scan lines in a single ultrasound image, L_v is the distance between samples of the two windowed RF echo segments in the axial direction, and L_i is the length of the 1-D RF window. Note that s_{avg} is not the actual strain but an effective strain that is being estimated because it is not always possible to know the exact stress being applied to the material. Therefore, the estimated strain value is the relative strain value of tissue components. The value of j in $r_2^{(i_s,j_s)}$ may deviate from j_s due to the expected lateral shift (Fig. 2). It is observed from Fig. 2 that if the column index j_s has a value (say, j_{s1}) in the pre-compression RF echo segment, then the post-compression RF echo segment will have a different column index. However, we can assume $j_s \approx j$ for low applied strain. Therefore, in selecting the post-compression signal window from the RF frame, Poisson's ratio is used to reduce the lateral shift effect in axial strain calculation while considering no lateral motion at the transducer face and at the supporting base with a closely satisfied non-slip boundary condition. For well-behaved axial stress, lateral motion is zero around the center of the application area and increases with increasing distance (Fig. 2).

After stretching the post-compression echo window $r_2^{(i_s,j_s)}$ by a factor δ (≤ 1), i.e., $r_\delta^{(i_s,j_s)}(i) = r_2^{(i_s,j_s)}(\delta i)$, the NCC coefficient $\zeta_\delta^{1D}(k)$ between $r_1^{(i_s,j_s)}$ and $r_\delta^{(i_s,j_s)}$ is calculated as [19]
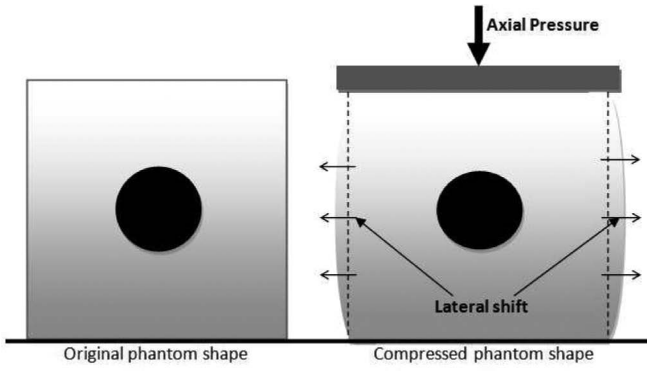
Fig. 2. Representation of lateral shift due to axial applied pressure in non-slip boundary condition. This lateral shift can be incorporated by using expected lateral shift from the Poisson's ratio in the selecting signal window.

$$\zeta_{\delta,\text{1D}}^{(i_s,j_s)}(k) = \frac{\sum_{i=1}^{L_i} r_1^{(i_s,j_s)}(i) \cdot r_\delta^{(i_s,j_s)}(i+k)}{\sqrt{\sum_{i=1}^{L_i}\{r_1^{(i_s,j_s)}(i)\}^2 \sum_{i=1}^{L_i}\{r_\delta^{(i_s,j_s)}(i)\}^2}}. \quad (7)$$

The peaks of $\zeta_{\delta,\text{1D}}^{(i_s,j_s)}(k)$ can be calculated by using any subpixel interpolation algorithm (e.g., cosine interpolation, parabolic interpolation) for different values of δ. However, in this work we have used parabolic interpolation. Therefore,

$$k_p = \arg\max_\delta\{\zeta_{\delta,\text{1D}}^{(i_s,j_s)}(k)\}, \text{ and} \quad (8)$$

$$M_\delta^{\text{1D}}(i_s, j_s) = \zeta_{\delta,\text{1D}}^{(i_s,j_s)}(k_p). \quad (9)$$

Here, M_δ^{1D} is a 2-D matrix consisting of the cross-correlation peaks. A weighting function $w^{(i_s,j_s)}(i_1, j_1)$ is defined so that the RF windowed segments of increasing distance are properly weighted to be less emphasized (Fig. 3). As the stiffness of a tissue element is more similar to the nearer neighboring elements than the distant ones, an exponential weight function is introduced that ensures relatively larger weights to the nearest cross-correlation peaks that decay rapidly with distance:

$$w^{(i_s,j_s)}(i_0, j_0) = e^{-|\chi_a(i_0 - i_s)| - |\chi_l(j_0 - j_s)|}, \quad (10)$$

where χ_a and χ_l are the weighting factors in the axial and lateral directions, respectively, and $i_s - L_a \leq i_0 \leq i_s + L_a$ and $j_s - L_l \leq j_0 \leq j_s + L_l$. It is clear from (10) that $w^{(i_s,j_s)}(i_0, j_0)$ has a maximum value of unity at $(i_0, j_0) = (i_s, j_s)$. To estimate the average strain, a cost function is defined from M_δ^{1D} (9) and weight function $w^{(i_s,j_s)}(i_0, j_0)$ as

$$J_\delta^{(i_s,j_s)} = \sum_{i_1 = i_s - L_a}^{i_s + L_a} \sum_{j_1 = j_s - L_l}^{j_s + L_l} w^{(i_s,j_s)}(i_1, j_1) M_\delta^{\text{1D}}(i_1, j_1), \quad (11)$$

where L_a and L_l are the nearest neighbor (NN) factors in the axial and lateral directions, respectively. Unless other-

wise specified, we use $L_a = 3$, $L_l = 3$ in this study. Increase in the value of L_a and L_l causes more smoothing of the strain image. $J_\delta^{(i_s,j_s)}$ is calculated for different values of δ ($\delta_{\min} \leq \delta \leq \delta_{\max}$). Generally, $\delta_{\max}$ is set to 1 (zero strain) and $\delta_{\min}$ is set to a lower value than $(1 - s_{\text{avg}})$. The desired value of δ is calculated for which $J_\delta^{(i_s,j_s)}$ is the maximum as

$$\delta_o^{(i_s,j_s)} = \arg\max_\delta\{J_\delta^{(i_s,j_s)}\}. \quad (12)$$

And, finally, the effective strain at (i_s, j_s) is estimated as

$$S_o(i_s, j_s) = 1 - \delta_o^{(i_s,j_s)}. \quad (13)$$

It is important that $\delta = \delta_o^{(i_s,j_s)}$ is indirectly partially dependent on the range of values of $M_\delta^{\text{1D}}(g_s, h_s)$ ($i_s - L_a \leq g_s \leq i_s + L_a$; $j_s - L_l \leq h_s \leq j_s + L_l$) via the cost function. It is a clear contrast to the instantaneous cost function-based approaches in adaptive spectral stretching or adaptive stretching-based strain estimation. Therefore, the neighboring cross-correlation peaks governed by the weight function have a significant impact in the calculation of $S_o(i_s, j_s)$, and estimated strain is expected to be much more well behaved.

Two significant advantages of the DASE compared with the conventional adaptive stretching-based strain estimation [7] can be summarized as

1) Reducing the lateral shift due to axial stress [using ν in (6)] before the selection of pre- and post-compression RF segments; and
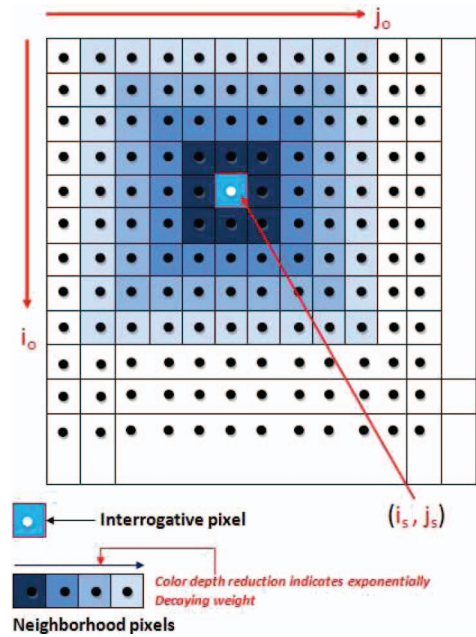

Fig. 3. Illustration of the neighboring window's contribution in the estimation of effective strain for a particular point (i_s, j_s) in the correlation peak map for a particular strain s. Note that some neighboring (here four) pixel values weighted exponentially are also used to estimate the effective strain at (i_s, j_s) point.

2) Estimating the average strain directly by taking the nearest neighbors into account.

Note that we also discuss a 2-D direct average strain estimation method in the next subsection. But the term DASE will, by default, indicate the 1-D direct average strain estimation, unless otherwise specified.

2) 2-D Direct Average Strain Estimation: In this method, we chose 2-D pre- and post-compression windows of three consecutive scan lines according to (5) and (6) with $\nu = 0$ (i.e., no incorporation of Poisson's ratio). After stretching the post-compression windowed signal in the axial direction, the NCC coefficient $\zeta_{\delta,2D}^{(i_s,j_s)}(k,p)$ is calculated as [19]

$$\zeta_{\delta,2D}^{(i_s,j_s)}(k,p) = \frac{A}{B}, \quad \text{where} \tag{14}$$

$$A = \sum_{i=1}^{L_i}\sum_{n=1}^{L_w} r_1^{(i_s,j_s)}(i,n) \cdot r_\delta^{(i_s,j_s)}(i+k,n+p),$$

$$B = \sqrt{\sum_{i=1}^{L_i}\sum_{n=1}^{L_w}\{r_1^{(i_s,j_s)}(i,n)\}^2\{r_\delta^{(i_s,j_s)}(i,n)\}^2},$$

where n denotes the scan-line index and L_w denotes the width of the 2-D windowed echo segment. The peaks of $\zeta_{\delta,2D}^{(i_s,j_s)}(k,p)$ are calculated by using the parabolic sub-pixel interpolation algorithm for different values of δ, and M_δ^{2D} is computed in a similar fashion as M_δ^{1D} (9). Similarly, the cost function for the 2-D case is defined as in (11) for the 1-D case by using the same weight function defined in (10). Finally, by finding the corresponding δ for the maximum cost, the average strain S_o at (i_s,j_s) is estimated for the 2-D case.

C. Elasticity Estimation from Average Displacement

The proposed DASE technique can generate very high-quality strain images as demonstrated in the results section, but at the cost of very high computational time like other published direct strain estimation techniques. Therefore, in spite of noise susceptibility, gradient-based strain estimation is more popular, especially for real-time and near-real-time implementations. In this technique, effective strain is calculated as the spatial derivative of the axial displacement. Various techniques are available in the literature to denoise the displacement field such as the smoothing spline method [6], least-squares approach [13], regularization-based approach [16], etc. Because noise is unavoidable in free-hand elastography, we develop here a robust algorithm for estimation of the average displacement. We assume that the displacement of the neighboring tissue elements along each of the A-lines at the same distance from the ultrasound probe would be the same in response to the equally applied external pressure.

In many gradient-based strain estimation techniques, post-compression echo is temporally stretched to reduce de-correlation. But this approach leads to increased noise

in stiffer lesion areas where the post-compression signal undergoes less compression. In our proposed GBASE method, we use two different values of δ (i.e., $\delta_{max} = 1$ and $\delta_{avg} = 1 - s_{avg}$) for stretching the post-compression signal to compute the cross-correlation $\zeta_\delta^{(i_s,j_s)}(k)$ (7). We have used $\delta_{max} = 1$ for the purpose of detecting hard objects (e.g., lesions) in the material being scanned. If a hard inclusion is present, then the post-compression RF echo signal will not be a compressed replica of the pre-compression one as assumed in the signal model. Therefore, to detect the hard inclusions we do not stretch the post-compression RF echo signal, and setting δ_{max} equal to 1 serves the purpose. Then, two cost functions are calculated as

$$\tilde{J}_\delta^{(i_s,j_s)}(k) = \sum_{j_1=j_s-L_1}^{j_s+L_1} w^{(i_s,j_s)}(i_s,j_1)\zeta_\delta^{(i_s,j_s)}(k), \tag{15}$$

where $\delta = \delta_{max}$ and δ_{avg}. We calculate the stretching factor δ via the strain s as $\delta = 1 - s$, and therefore, the δ_{max} corresponds to the no compression (strain) case and the δ_{avg} corresponds to the approximate applied strain case. From the maximum of the cost functions, the displacement is calculated as

$$k_\delta^{(i_s,j_s)} = \arg\max_k\{\tilde{J}_\delta^{(i_s,j_s)}(k)\}, \quad \text{for } \delta = \delta_{max} \text{ and } \delta_{avg}. \tag{16}$$

Finally, the displacement matrix is calculated as

$$D(i_s,j_s) = \begin{cases} k_{\delta_{avg}}^{(i_s,j_s)} + k_{comp} + \dfrac{L_i}{2}s_{avg}, & \beta \geq \gamma \\ k_{\delta_{max}}^{(i_s,j_s)} + k_{comp}, & \text{otherwise} \end{cases} \tag{17}$$

where $\beta = \tilde{J}_{\delta_{avg}}^{(i_s,j_s)}(k_{\delta_{avg}}^{(i_s,j_s)})$, $\gamma = \tilde{J}_{\delta_{max}}^{(i_s,j_s)}(k_{\delta_{max}}^{(i_s,j_s)})$, and $k_{comp} = \text{round}((i_s - 1)\delta_{avg}L_v) - i_s - 1)L_v$. Here, k_{comp} is inserted to compensate the effect of using the shifting factor $(1 - s_{avg})$ for the window selection in (6). As we stretch the post-compression signal before cross-correlation operation, we used the third part $((L_i/2)s_{avg})$ in (17) to incorporate the effect of signal stretching on echo displacement. Finally, the effective strain $S_g(i_s,j_s)$ is calculated from $D(i_s,j_s)$ using the least-square-error-based strain estimation method [13] with four points per strain estimate.

In the cost functions (15) above, we can use an error function that defines the conservation of echo amplitude to avoid relatively computationally expensive NCC-based shift measurements (7). A simple sum of absolute differences (NSAD) or the sum of squared differences (NSSD) [19] between the pre- and stretched post-compression RF segments can be also used to calculate the error function as in the following:

$$\zeta_\delta^{(i_s,j_s)}(k) = \sum_{i=1}^{L_i}\left[\frac{r_1^{(i_s,j_s)}(i)}{\sqrt{\sum_{i=1}^{L_i}r_1^{(i_s,j_s)}(i)^2}} - \frac{r_\delta^{(i_s,j_s)}(i+k)}{\sqrt{\sum_{i=1}^{L_i}r_\delta^{(i_s,j_s)}(i)^2}}\right]^\gamma, \tag{18}$$

where γ (= 1 for NSAD and = 2 for NSSD) is a constant. However, it is well established that NSSD performs better than NSAD. The cost function in (15) shall be minimized in this case.

III. Simulation and Experimental Results

We first present the efficacy of different salient features of the proposed methods. Then, we provide comparative results of our proposed methods with the adaptive strain estimator (AS) for elastography [7] and analytic minimization (AM) [16] method using the FEM phantom, CIRS experimental phantom and the *in vivo* patient data. In addition to subjective evaluation by visual inspection, we compare the performances of different methods in terms of several numerical metrics: elastographic signal-to-noise ratio (SNRe) [20], elastographic contrast-to-noise ratio (CNRe) [21], peak signal-to-noise ratio (PSNR), and mean structural similarity (MSSIM) [22].

A. Effectiveness of the Salient Features of the Proposed Methods

We use the FEM simulation phantom for checking the performance of different salient features of the proposed methods. A rectangular 40×40 mm FEM phantom was simulated using the analysis software Algor (Algor Inc., Pittsburgh, PA). In this simulation, the total number of nodes was $30\,372$. A 2-D FEM model was used, and therefore, it did not model out-of-plane motion. Total number of scatterers used in the simulation was $30\,372$. This phantom had a homogeneous background with stiffness of 60 kPa with four circular inclusions of 7.5 mm diameter each [Fig. 4(a)]. The stiffness of the four inclusions were as follows: (a) the bottom left one was 10 dB stiffer, (b) the top one was 20 dB stiffer, (c) the bottom right one was 30 dB stiffer, and (d) the middle one was 40 dB stiffer than the background. The phantom was compressed from the top using a larger-width planar compressor. The phantom was placed on a planar surface and allowed to freely expand (free-slip condition at top and bottom surfaces). An ultrasonic transducer of center frequency, f_0

= 5 MHz and bandwidth = 60%, was used to scan the phantom from the top by a non-diffracting beam of width = 1.5 mm. The total number of scan lines was 128. Sonographic SNR of 40 dB [6] was simulated with the addition of zero-mean white noise. Fig. 4(b) shows the ideal elastogram for 2% applied strain. The ideal strain profile of the marked line in Fig. 4(b) is plotted in Fig. 4(c), and we observe that there are two well-defined strain wells due to 10 and 30 dB lesions indicating very small strain values in lesion regions. This strain profile also indicates that there are strain variations in the background region due to interaction between lesions, although the phantom has a uniform stiffness background.

To show the efficacy of Poisson's ratio, first we generate the baseline strain image [Fig. 5(a)] using the conventional adaptive stretching-based concept [7] by setting $\nu = 0$ (i.e., not using Poisson's ratio to reduce the lateral shift effect) to select the RF window segment in (6) and $L_a = L_l = 0$ (i.e., not taking advantage of using the physical proximity of neighborhood) in computing the cost function in (11). The image in Fig. 5(a) is severely distorted. Now, setting $\nu = 0.25$ arbitrarily and $L_a = L_l = 0$, we generate Fig. 5(b) to demonstrate the reduction of noise that can be achieved in the left and right boundaries. The Poisson's ratio used in the simulation of the FEM phantom is 0.495, and therefore, the selection of $\nu = 0.25$ does not generate noise-free strain image though the noise is reduced significantly. The impact of using the NN factor is observed in Fig. 5(c). In Fig. 5(c), we get an almost noise-free image for using the NN factor by setting $L_a = L_l = 3$. Note that the built-in smoothing by using the NN factor gives much better results than that of the median smoothing result in Fig. 5(d). Also note that the performance of the proposed method is sensitive to the setting of the Poisson's ratio for a large applied strain. Moreover, if the assumed Poisson's ratio is of the order of the true value, e.g., $0.5\nu_{vt} \leq \nu \leq 1.5\nu_{vt}$ (where ν_{vt} is true Poisson's ratio) at high strain, then NN factor would not affect the perceptual quality of the strain image noticeably.

To demonstrate the efficacy of the proposed cost function, we plot the mean of the NCC peaks $M_\delta^{1D}(g_s, h_s)$ ($i_s - 1 \leq g_s \leq i_s + 1$ and $j_s - 1 \leq h_s \leq j_s + 1$) and the proposed cost function ($J_\delta^{(i_s, j_s)}$) for strain map at (i_s, j_s) against
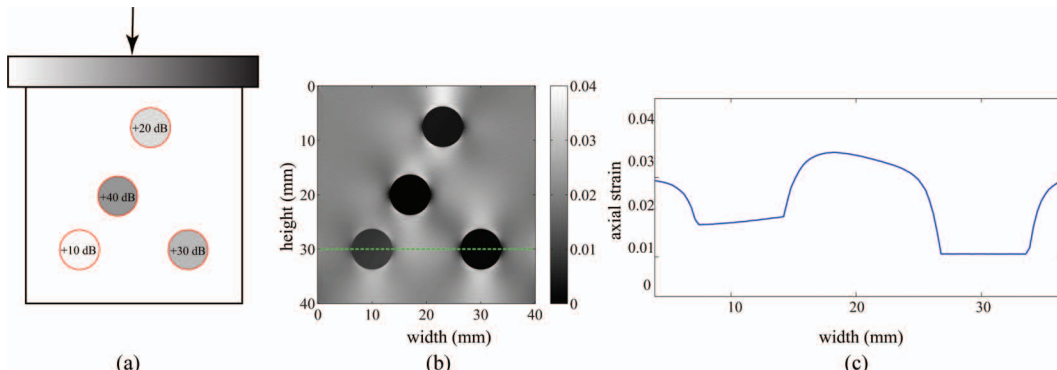

Fig. 4. FEM simulation phantom. (a) Stiff inclusions in a homogeneous background of 60 kPa, (b) corresponding ideal elastogram, (c) strain profile of the marked line in (b).

the applied axial strain in Fig. 6. Twenty-five realizations of the FEM phantom described in Fig. 4(a) under 8% applied strain are used to generate Fig. 6. We can see from Fig. 6 that the abscissa of the mean NCC peak conventionally used for the instantaneous strain estimation at (i_s, j_s) is much deviated from the expected strain value (i.e., 0.08). But the strain value at the maximum of the mean cost function $(J_\delta^{(i_s, j_s)})$, defined from the NCC peaks of the interrogative window and its neighborhood, is exactly equal to the approximate applied strain 0.08. In addition, the standard deviation of the cost peak is much lower than that of the instantaneous NCC peak. This shows a clear advantage of using the proposed cost function rather than using the instantaneous NCC peaks to calculate the strain.

Like the proposed DASE technique, the proposed GBASE method has the built-in smoothing feature in the displacement domain. If no lateral windows are considered in displacement estimation [i.e., $L_l = 0$ in (15)], then the instantaneous estimate of the displacement is obtained and is shown in Fig. 7(a). The displacement field is not smooth as evident from the zoomed view in Fig. 7(a). On the contrary, as shown in Fig. 7(b), it is smooth and continuous when the lateral windows ($L_l = 5$) are also considered in the displacement estimation of the interrogative window.

Along with the smoothing approach, the proposed GBASE method has another notable difference with the conventional gradient-based strain estimators; it uses two different temporal stretching in the estimation of the displacement matrix. Fig. 8(a), (b) now demonstrates the effect of two types of temporal stretching on the estimated strain images. Fig. 8(a) shows a strain image generated by the proposed GBASE method using only one stretching factor (δ_{avg}). In this generated strain image, the hard inclusions are not appearing clearly. But if we use two stretching factors, then the hard inclusions are visualized clearly as evident from Fig. 8(b).

B. Comparison Using FEM Simulation

Before presenting the comparative results, we provide the definitions of four numerical performance metrics, e.g., SNRe, CNRe, PSNR, and MSSIM. The quality metrics are defined as SNRe [20]:

$$\text{SNRe} = \frac{\mu_s}{\sigma_s}, \tag{19}$$

where μ_s and σ_s denote the statistical mean and standard deviation of the strain computed in a homogeneous area, respectively.

CNRe [21] is defined as follows:

$$\text{CNRe} = \frac{2(\mu_l - \mu_b)^2}{\sigma_l^2 + \sigma_b^2}, \tag{20}$$

where μ is the mean strain and σ is the standard deviation of the strain in a homogeneous area. The sub-subscripts l and b refer to the lesion and background, respectively. PSNR is defined as follows:

$$\text{PSNR} = 20 \log_{10}\left(\frac{M_I}{\sqrt{(\text{MSE})}}\right)\text{dB}, \tag{21}$$

$$\text{where MSE} = \frac{1}{PQ} \sum_{p=0}^{P-1}\sum_{q=0}^{Q-1}[S_X(p,q) - S_Y(p,q)]^2, \tag{22}$$

where $S_X|_{P \times Q}$ and $S_Y|_{P \times Q}$ are the actual and estimated strain images, respectively, and M_I is the dynamic range of the strain image.

The MSSIM is shown to be an excellent predictor of the image perceptual quality. It considers contrast, luminance, and structural similarity between the estimated and actual strain images to compute the value of the index. For calculating the MSSIM index, at first the actual and estimated strain images are locally windowed. Each of the windowed actual and estimated signals, $x(x = [x_1\, x_2\, \ldots\, x_N])$ and $y(y = [y_1\, y_2\, \ldots\, y_N])$, respectively, are of length N. Then these two signal vectors are Gaussian function $w(w = [w_1\, w_2\, \ldots\, w_N])$ weighted, with a standard deviation of 1.5 samples, where $\sum_{i=0}^{N} w_i = 1$. Then the estimates of local statistics of x and y are calculated as

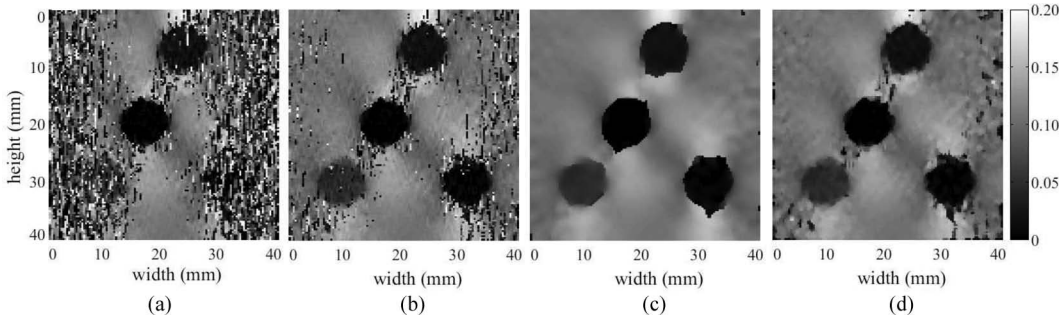$$\mu_x = \frac{1}{N} \sum_{i=1}^{N} w_i x_i, \tag{23}$$

Fig. 5. Effect of Poisson's ratio (ν) and lateral and axial NN factors in the strain estimation. Strain images generated by the (a) conventional direct strain estimator [7] for 10% applied strain, (b) proposed DASE method (using $\nu = 0.25$ and $L_a = L_l = 0$) for 10% applied strain, (c) proposed DASE method (using $\nu = 0.25$ and $L_a = L_l = 3$) for 10% applied strain, (d) median filtered strain image of (b).
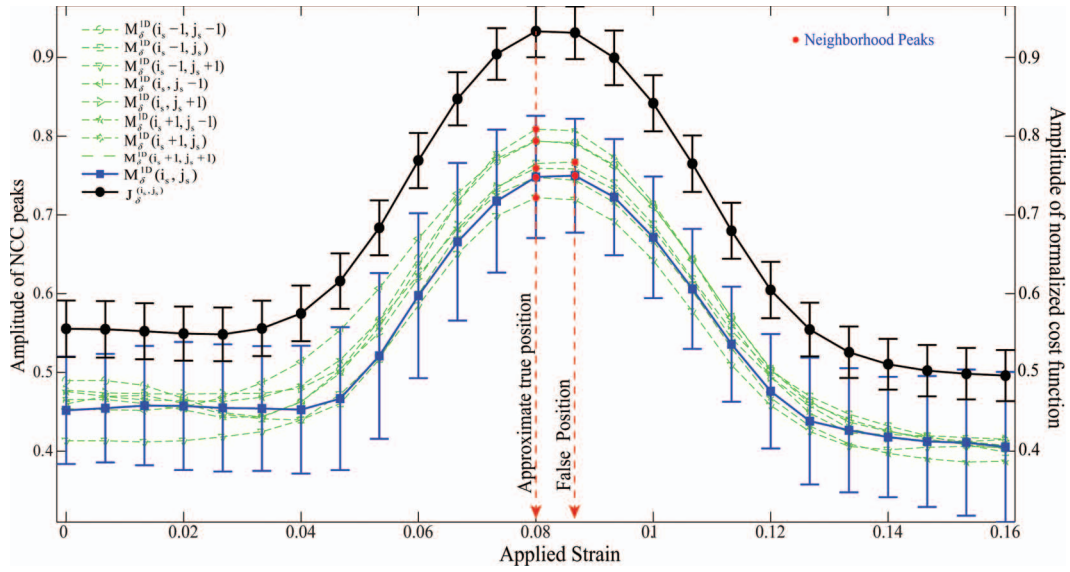
Fig. 6. Representation of instantaneous mean NCC peaks $M_\delta^{1D}(g_s, h_s)$ ($i_s - 1 \leq g_s \leq i_s + 1$ and $j_s - 1 \leq h_s \leq j_s + 1$) and the proposed mean cost function ($J_\delta^{(i_s, j_s)}$) for strain map at (i_s, j_s) using FEM phantom (under 8% applied strain) against the applied strain. We use 25 different speckle/noise realizations to generate error bar plots.

$$\mu_y = \frac{1}{N}\sum_{i=1}^{N} w_i y_i, \tag{24}$$

$$\sigma_x = \sqrt{\frac{1}{N-1}\sum_{i=1}^{N} w_i(x_i - \mu_x)^2}, \tag{25}$$

$$\sigma_y = \sqrt{\frac{1}{N-1}\sum_{i=1}^{N} w_i(y_i - \mu_y)^2}, \tag{26}$$

$$\sigma_{xy} = \frac{1}{N-1}\sum_{i=1}^{N} w_i(x_i - \mu_x)(y_i - \mu_y). \tag{27}$$

The SSIM index between the signals $x(x = [x_1\, x_2\, \ldots\, x_N])$ and $y(y = [y_1\, y_2\, \ldots\, y_N])$ is calculated as [22]

$$\text{SSIM} = \frac{(2\mu_x\mu_y + C_1)(2\sigma_{xy} + C_2)}{(\mu_x^2 + \mu_y^2 + C_1)(\sigma_x^2 + \sigma_y^2 + C_2)}, \tag{28}$$

where $C_1 = (K_1 M_I)^2$, $C_2 = (K_2 M_I)^2$, $K_1 = 0.01$, and $K_2 = 0.03$. Here, M_I is the dynamic range of the pixel values. Finally, the mean SSIM (MSSIM) is calculated as

$$\text{MSSIM} = \frac{1}{M}\sum_{j=1}^{M} \text{SSIM}(x_j, y_j), \tag{29}$$

where x_j and y_j are the image contents at the jth local window and M is the number of local windows in the image.

The four numerical performance metrics are calculated for different applied strains (1 to 8%) on 25 realizations of the FEM simulation phantom. The calculated values are graphically presented with error bars in Fig. 9(a)–(g). The SNRe values indicate that our proposed methods (DASE, 2-D DASE, and GBASE) perform significantly better than the previous AS and AM methods. Although the AM method shows better performance than the AS method for
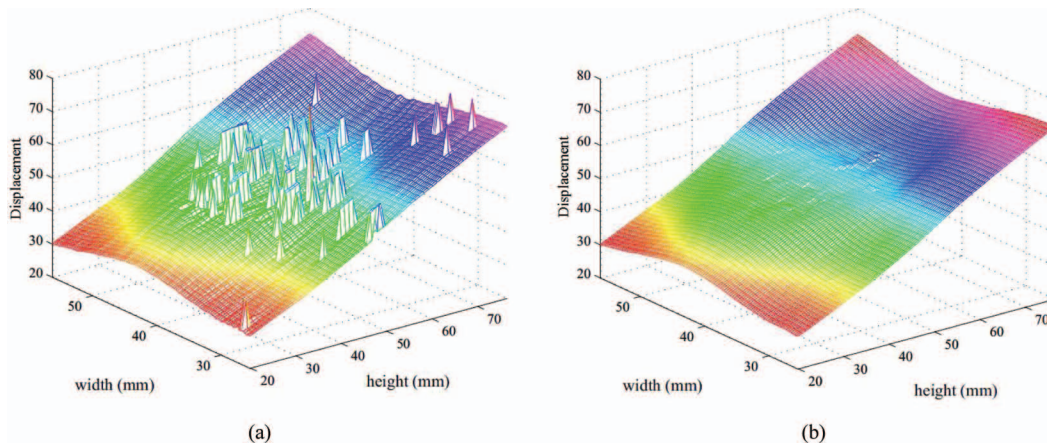

Fig 7. Effect of lateral NN factor in the displacement estimation. Displacement images generated by the proposed GBASE method using $L_1 = 0$ for 3% applied strain (a) and the proposed GBASE method using $L_1 = 5$ for 3% applied strain (b).
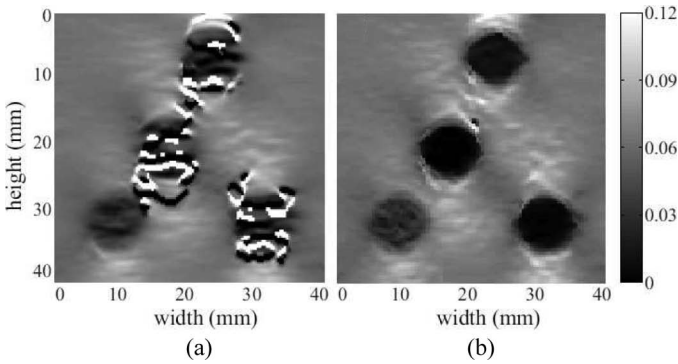
Fig. 8. Effect of two stretching factors in the strain estimation. Strain images generated by the (a) proposed GBASE method using only one stretching (δ_{avg}) for 4% applied strain, (b) proposed GBASE method using two stretching factors (δ_{avg} and δ_{max}) for 4% applied strain. For both cases, Poisson's ratio, $\nu = 0.5$, is used.

up to 2% applied strain, the SNRe of the AM method falls sharply at higher strains. In Fig. 9(b), although the PSNR values of the AS method are better than that of the proposed GBASE method at high strain, the DASE and 2-D DASE methods show significantly better performance. Like the SNRe, the PSNR of the AM method also falls at higher strains. From the MSSIM values in Fig. 9(c), we see that the DASE, 2-D DASE methods perform significantly better and the GBASE method performs much better than the AS method. The AM method shows as usual poor performance at higher strains. For the conventional methods, generally there is a decreasing trend of the quality metrics with increasing strain. But the SNRe, PSNR, and MSSIM values are more consistent from low to high strains for the proposed DASE and 2-D DASE methods, indicating the robustness of the methods to decorrelation noise. In Figs. 9(d)–(g), we plot the CNRe values for four lesions of different stiffness in the FEM phantom. For the 10 and 20 dB lesions [Figs. 9(d)–(e)], CNRe of the proposed GBASE method is comparable to that of the AS method and much better than the AM method; the proposed DASE and 2-D DASE methods significantly outperform the other methods and display an increasing trend in CNRe with the increase of applied strain. However, for the 30 and 40 dB lesions [Figs. 9(f)–(g)], the CNRe values of all the proposed methods show significantly better performance than the AS and AM methods. The results in Figs. 9(f)–(g) also indicate that the GBASE method is particularly suitable for detecting the stiffer lesions. Because of excessive smoothing, the CNRe values of the AM method are the lowest. We also observe that the AM method is very sensitive to the setting of the tuning parameters. The presented results are due to the choice of most suitable parameters.

For a qualitative evaluation of the perceptual quality of the strain images generated by the AS, AM, and proposed GBASE and DASE methods, we present strain images of the FEM simulation phantom for four (2, 4, 6, and 8%) different applied strains in Fig. 10. In all the analyses, we have used a data window (L_l) of size 2.28 mm and an

inter-window shift (L_v) of 0.28 mm. We have also used different values of NN factors ($L_a = L_l = 1$ and $L_a = L_l = 3$) for generating strain images by the DASE method. Thus, for 2% strain, all the methods produce satisfactory images, although the AS and AM methods produce somewhat noisier strain images. For 6 and 8% strains, images generated by the AS method is significantly distorted in left and right boundaries and the strain images generated by the AM method are severely distorted. For the AM method, the inclusions except the 40 dB are nearly invisible at higher applied strains. For the AS method, the strain image is noisy at 8% strain and the 10- and 30-dB lesions cannot be clearly observed. The GBASE method produces good quality strain images for low strains. At high applied strains, although the inclusion boundaries are distorted, the inclusions are clearly distinguishable from the homogeneous background. In contrast, the DASE method for both NN factors generates very clean strain images at all strains from 2 to 8%, indicating the superiority of this method. We notice from these figures that we can control the degree of smoothing by changing the NN and weighting factors, which in turn gives us control over spatial resolution. Spatial resolution can be improved by reducing the value of NN factors. Though increasing the NN factors somewhat reduces the spatial resolution, the generated strain images for high NN factors are more noise free.

To observe the distortion in the strain image, horizontal 1-D strain profiles are depicted for two different applied strains in Fig. 11 for the AS, AM, and proposed methods. The profiles are selected so that the variation of stiffness in the 10- and 30-dB lesions is included [dashed horizontal line in Fig. 4(b)]. We have calculated two parameters from this strain plot. The first one is the total MSE between the ideal and the estimated strain profile and the second parameter is the lesion width. The true width of both the lesions is 7.50 mm. The estimated values of these quantities by different methods are shown in Tables II and III for 2 and 8% applied strain, respectively. From Tables II and III, it is clear that the total MSE is the least for the proposed DASE method with $L_a = L_l = 3$ for both the cases. The estimated widths for the 10- and 30-dB lesions are more accurate for the DASE method with $L_a = L_l = 1$ and the DASE method with $L_a = L_l = 3$ for low strain (2%) and high strain (8%), respectively. We note that the AS method can be considered a special case of the DASE method with $L_a = L_l = 0$ and $\nu = 0$. Thus, the use of nonzero NN factors significantly improves MSE. In addition, by decreasing the NN parameters (L_a, L_l) for low strain, we can improve spatial resolution (lesion width) at little cost to the MSE. However, due to increased decorrelation noise at high strain, higher L_a and L_l parameters improve performance. Regarding the gradient-based strain estimation techniques for low strain (2%), although the spatial resolution in terms of lesion widths is slightly better for the GBASE method than the AM method, at high applied strain (8%), the AM method completely fails whereas the GBASE method performs well.
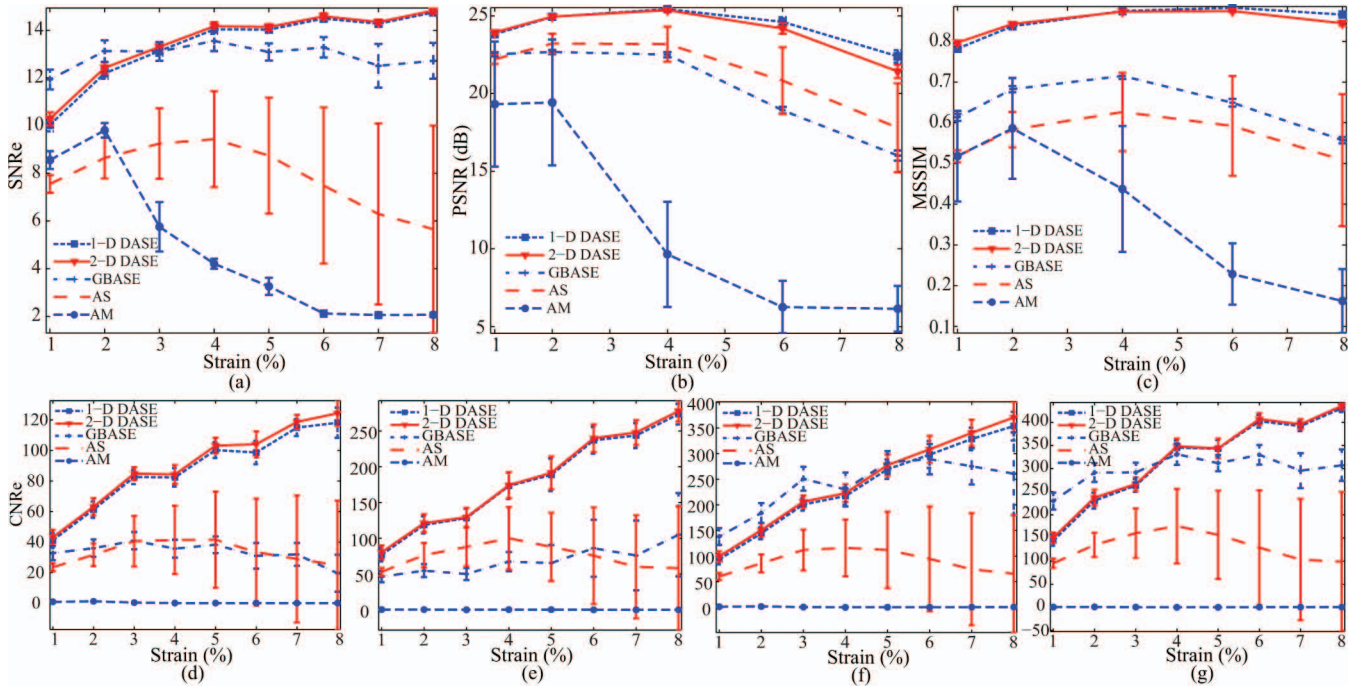
Fig. 9. Performance comparisons of different methods using numerical performance metrics. (a) SNRe vs. applied strain, (b) PSNR vs. applied strain, (c) MSSIM vs. applied strain, and CNRe vs. applied strain for (d) 10 dB, (e) 20 dB, (f) 30 dB, and (g) 40 dB lesions.

Thus, we can significantly increase the SNR of the strain images (in turn reduce the MSE) with little reduction in spatial resolution. Moreover, we can control the degree of the spatial resolution by changing the NN and weighting factors.

C. Comparison Using Experimental Phantom

We performed elastography experiments with a tissue-mimicking (TM) phantom of dimensions 90 × 90 × 120 mm with a 3-times stiffer (compared with the surrounding) cylindrical inclusion of 2-cm diameter (CIRS Inc., Norfolk, VA). An ATL (Bothell, WA) Ultramark 9 scanner with a 7.5-MHz linear-array transducer was used to acquire RF echo-signals from this CIRS phantom. The RF-echo data were sampled at 20 MHz and quantized at 14 bits/sample and we upsampled it to 50 MHz before processing in the digital domain. Time-gain-control (TGC) data were acquired, and before processing the RF data were corrected for TGC to simulate the condition in a clinical ultrasound machine. Although TGC is not necessarily a linear function in the way it affects the RF data, the performance of our strain estimator for this phantom data are observed to be very much insensitive to this correction.

Fig. 12(a)–(p) demonstrate the strain images generated by the AS, AM, proposed GBASE, and proposed DASE methods for four different applied external forces. The strain images for four different compressions indicate that the DASE method performs the best among all the methods being compared, though some noise is observed in Fig. 12(p) at 6% applied strain. In contrast, for 6% applied

strain, the AM method generates almost a null image. The strain images produced by the AS and GBASE methods are too noisy at 6% applied strain but perform well up to 4% applied strain.

In Fig. 13, we provide a quantitative comparison of the proposed methods with the AS and AM methods for this experimental phantom. Because the ideal strain image for this phantom cannot be obtained, the PSNR and MSSIM performance metrics cannot be calculated. Thus, we compare the performances of different methods using SNRe and CNRe. The variation of these two performance metrics are shown in Fig. 13 for the proposed, AS, and AM methods. The DASE performs the best among all other methods for both performance metrics. The GBASE method shows higher SNRe than the AS and AM methods, but the CNRe of the AS method is slightly greater than the GBASE method. As evident from Fig. 13, the AS, GBASE, and DASE methods are all superior to the AM method in terms of both the performance metrics.

D. Comparison Using in vivo Breast Data

The *in vivo* breast data used in the work were chosen from a database of 33 cases (age: 20 to 75 years). These data were acquired with free-hand compression and include both fibroadenomas and cancers. Benign and malignant cases were confirmed by histopathological reports. These data were acquired by using a Sonix SP500 (Ultrasonix Medical Corporation, Richmond, BC, Canada) scanner integrated with a L14–5/38 probe operating at 10 MHz (nominal) at the University of Vermont Medical Center. The study was approved by the institutional
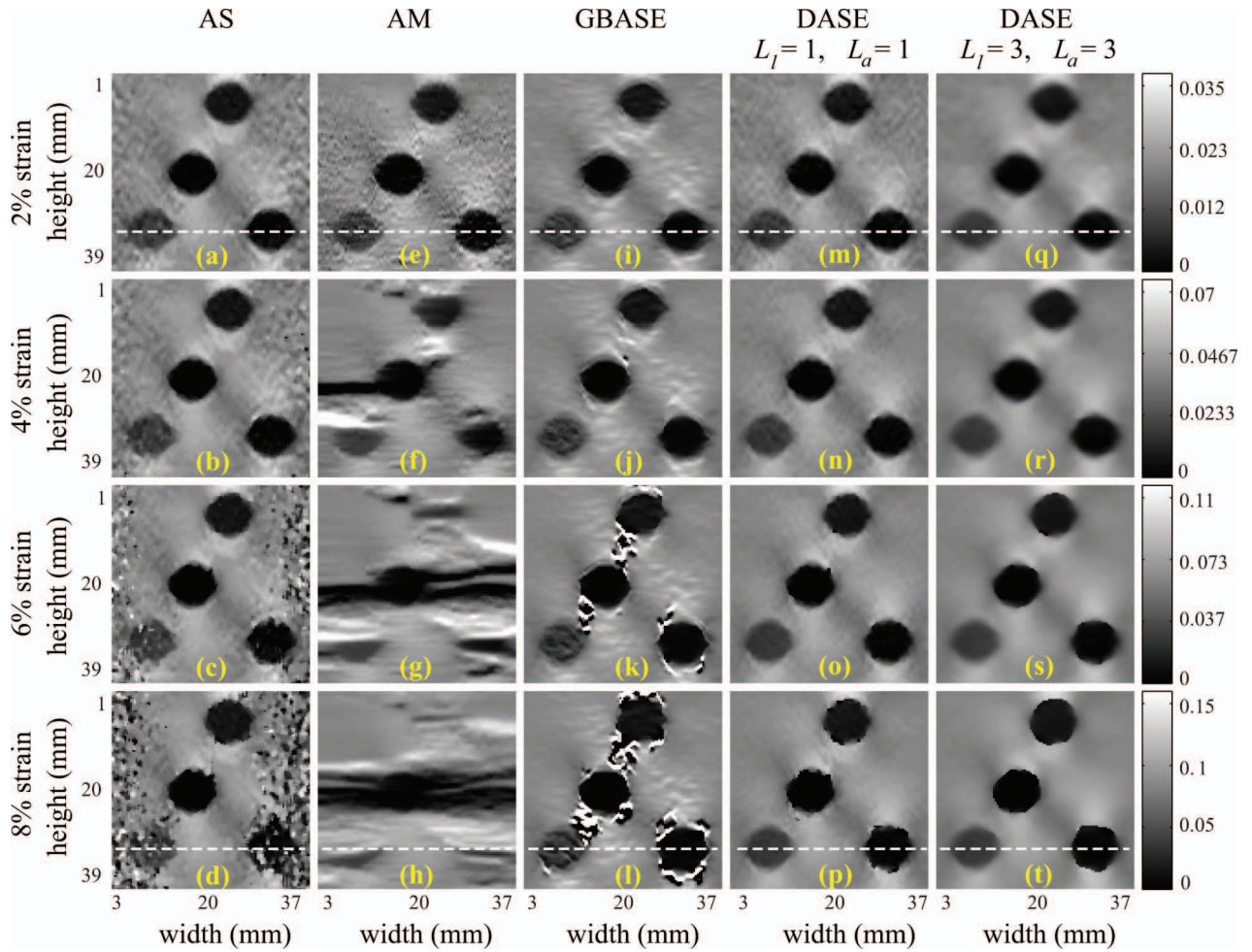
Fig. 10. Strain images of the FEM simulation phantom generated by different methods. Results (a)–(d) are produced by the AS, (e)–(h) are produced by the AM, (i)–(l) are produced by the proposed GBASE ($L_l = 3$, $\chi_1 = 0.25$, $\nu = 0.5$), (m)–(p) are produced by the proposed DASE ($L_a = 1$, $L_l = 1$, $\chi_a = \chi_1 = 0.25$, $\nu = 0.5$), and (q)–(t) are produced by the proposed DASE ($L_a = 3$, $L_l = 3$, $\chi_a = \chi_l = 0.25$, $\nu = 0.5$).

review board, and informed consent was obtained from every patient. Out of thirty-three cases, four are selected in this work. Three represent malignant breast tumors and the other one represents a benign case. The associated B-mode images of patient I (age 28, tumor type: fibroadenoma), patient II (age 38, tumor type: adenocarcinoma), patient III (age 63, tumor type: adenocarcinoma), and patient IV (age 58, tumor type: adenocarcinoma) are shown in Figs. 14(a), (f), (k), and (p), respectively. Malignant breast lesions appear smaller in ultrasonic B-mode images than in elastograms [23]; for fibroadenoma, they generally are larger or similar in size in B-mode images. From Figs.

14(a)–(e), it is clear that the lesion size in B-mode and strain images are almost the same as expected. Note that we do not know the approximate applied strain (s_{avg}) for *in vivo* data. To estimate this, we choose a region from the background data and calculated NCC peaks of multiple pre- and post-compression RF echo windows selected from that region for a large range of strain. These peaks are averaged for the corresponding strain value and the position of the maximum average peak is chosen as s_{avg}. Figs. 14 (b)–(e), (g)–(j), (l)–(o), and (q)–(t) show the strain images produced by the AS, AM, and proposed GBASE and DASE methods, respectively. We observe from these fig-

TABLE II. TOTAL MSE AND LESION WIDTH FOR THE 10 AND 30 dB INCLUSIONS FOR 2% APPLIED STRAIN.

	Total MSE ($\times 10^{-6}$)	Lesion width (mm)	
		10 dB	30 dB
AS	2.9757	7.50	7.55
AM	11.311	7.56	7.56
GBASE	2.9066	7.55	7.52
DASE with $L_a = L_l = 1$	2.1564	7.52	7.53
DASE with $L_a = L_l = 3$	1.9411	7.56	7.54

True lesion width is 7.50 mm.

TABLE III. TOTAL MSE AND LESION WIDTH FOR THE 10 AND 30 dB INCLUSIONS FOR 8% APPLIED STRAIN.

	Total MSE ($\times 10^{-6}$)	Lesion width (mm)	
		10 dB	30 dB
AS	100.47	7.58	4.18
AM	113.12	7.04	—
GBASE	11.843	7.56	7.59
DASE with $L_a = L_l = 1$	7.0589	7.57	7.58
DASE with $L_a = L_l = 3$	3.0905	7.54	7.55

True lesion width is 7.50 mm.

ures that the AM method can generate a useful strain image only for patients III and IV, though the lesion sizes are not accurate. All the other methods are fairly successful in visualizing the lesions from the backscattered ultrasound RF signals for patients I–III. As stated before, the size of the malignant (adenocarcinoma) object in the strain image is found larger than that in the B-mode image for our malignant cases [Figs. 14(f), (k), (p)]. It is clear that the contrast and depicted border of the cancerous tissue in our proposed GBASE method are better than those in the strain images generated by the other algorithms. The proposed DASE method shows the smoothest background with distinguishable lesion compared with the other approaches. The most interesting case among these four patients is the last case (patient IV). This patient suffers from adenocarcinoma with a very small lesion. This small lesion is not visible in the B-mode image [Fig. 14(p)]. We observe that only the GBASE method identifies the lesion clearly and with high contrast, whereas the other methods show the lesion but with an unclear boundary. Note that the strain images for patient IV *in vivo* breast data are estimated at sufficient low strain. Therefore, for the detection of small lesions, GBASE outperforms direct strain estimation methods (e.g., AS and DASE).

We also have plotted the 1-D strain for patients III and IV in Fig. 15 for a better understanding of the efficacy of the proposed methods. The heights of the lesions

mentioned in the histology report are 11 and 3 mm for patients III and IV, respectively. The 1-D strain plot in Fig. 15(a) indicates that the strain variation for the AM, proposed GBASE, and DASE methods are free from abnormal jumps. The width of the strain well for the AM method is smaller than the GBASE and DASE methods, which is a clear mismatch with the histology report. It is found from Fig. 15(a) that the estimated heights of the lesion for the AS, AM, GBASE, and DASE methods are 6.17, 11.26, 11.18, and 11.28 mm, respectively. However, it is almost impossible for an automated detection system to accurately detect the height of the lesion by the AS method because the AS method produces an abnormal jump inside the strain well. Therefore, it can be said that the proposed methods outperform the AS method in detecting lesions or for estimating the size of the lesions. On the other hand, only the GBASE method demonstrates a clear strain well for patient IV *in vivo* breast data, and the estimated lesion height is 3.07 mm (close to the histology report that reveals 3 mm).

E. Evaluating Performance in Terms of Computation Time

A comparison of the four (AM, AS, DASE, and GBASE) methods in terms of computation time reveals that the displacement-based AM method requires the shortest time
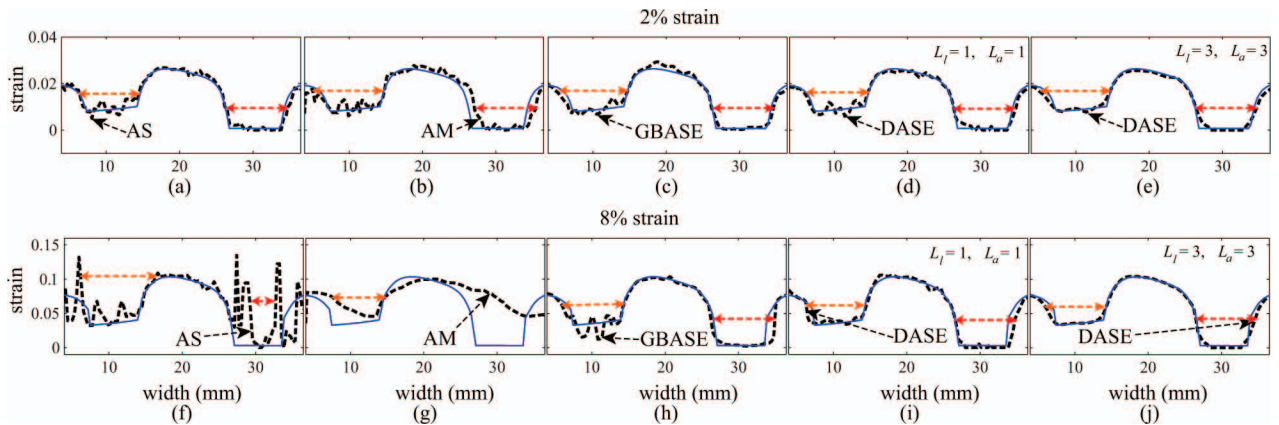

Fig. 11. Strain curves generated for the FEM simulation phantom at 2% and 8% applied strain by using different methods. (a)–(e) Lateral strain profile for 2% applied strain at a depth of 30.7 mm that includes the 10 and 30 dB inclusions. Comparisons with ideal strain curve are shown for (a) AS, (b) AM, (c) proposed GBASE (d) proposed DASE for $L_a = L_l = 1$, $\nu = 0.5$ (e) proposed DASE for $L_a = L_l = 3$, $\nu = 0.5$. (f)–(i) Lateral strain profile for 8% applied strain at a depth of 30.7 mm that includes the 10 and 30 dB inclusions. Comparisons with ideal strain curve are shown for (f) AS, (g) AM, (h) proposed GBASE, (i) proposed DASE for $L_a = L_l = 1$, $\nu = 0.5$, (j) proposed DASE for $L_a = L_l = 3$, $\nu = 0.5$.
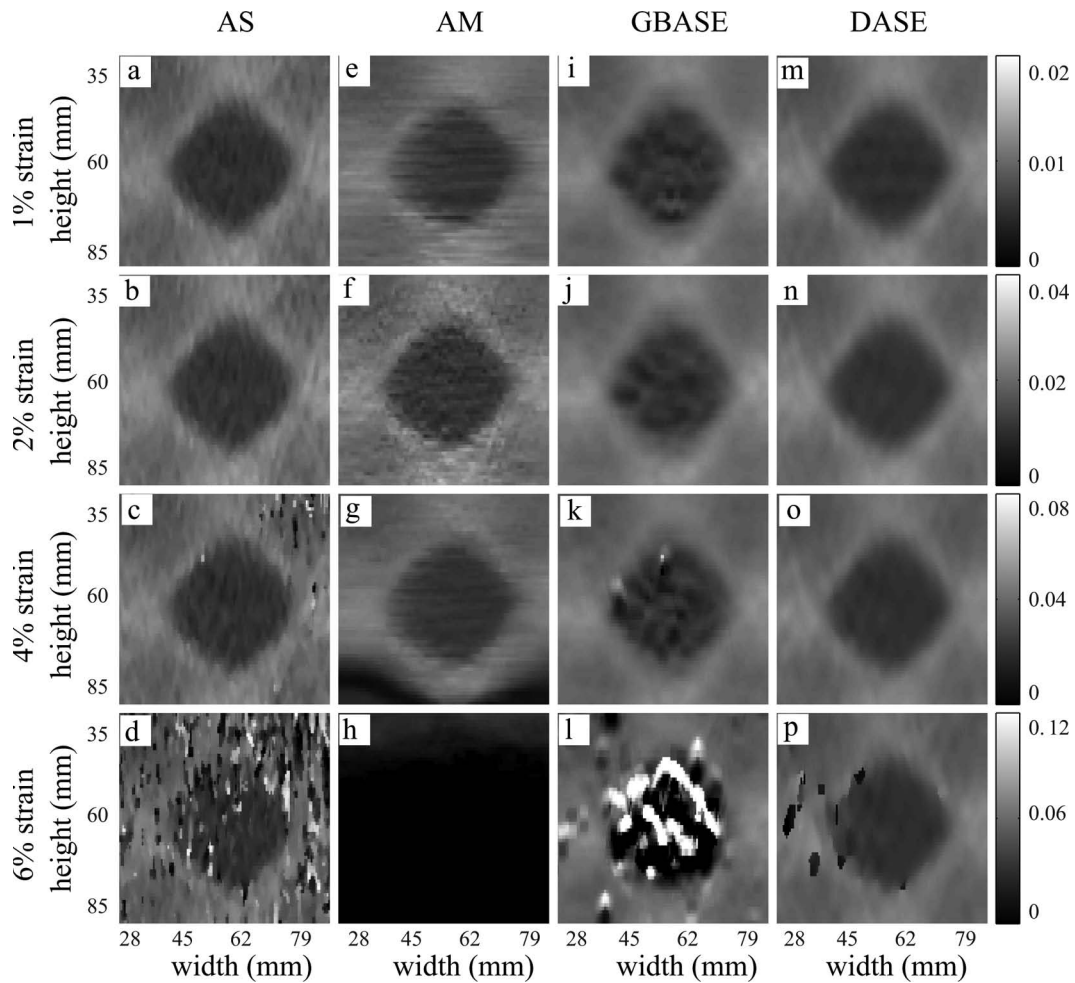
Fig. 12. Strain images of the experimental phantom generated by different methods. Results (a)–(d) are produced by the AS method, (e)–(h) are produced by the AM method, (i)–(l) are produced by the proposed GBASE ($L_a = 3$, $\chi_1 = 0.25$, $\nu = 0.5$), and (m)–(p) are produced by the proposed DASE ($L_a = 3$, $L_l = 3$, $\chi_a = \chi_1 = 0.25$, $\nu = 0.5$).

to generate the strain image. On the other hand, the AS and DASE methods take comparatively greater time than that of GBASE method. The computation time (CPU: Core 2 Duo, 2.5 GHz, RAM: 2 GB, software: MATLAB, The MathWorks, Natick, MA) of our implementation of the AM, AS, DASE, and GBASE methods for generating the strain images (*in vivo* breast experiment: patient I) are 1.41, 197.83, 200.47, and 31.87 s, respectively. Note, how-
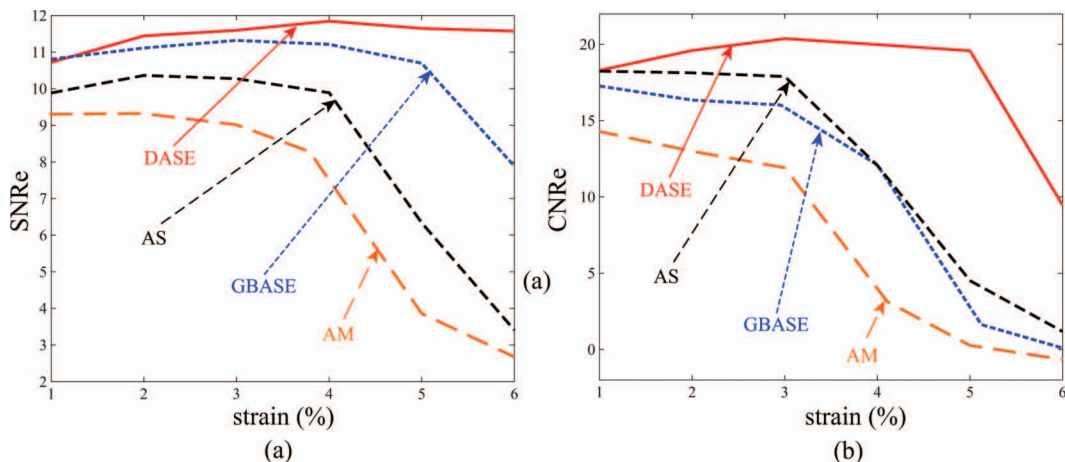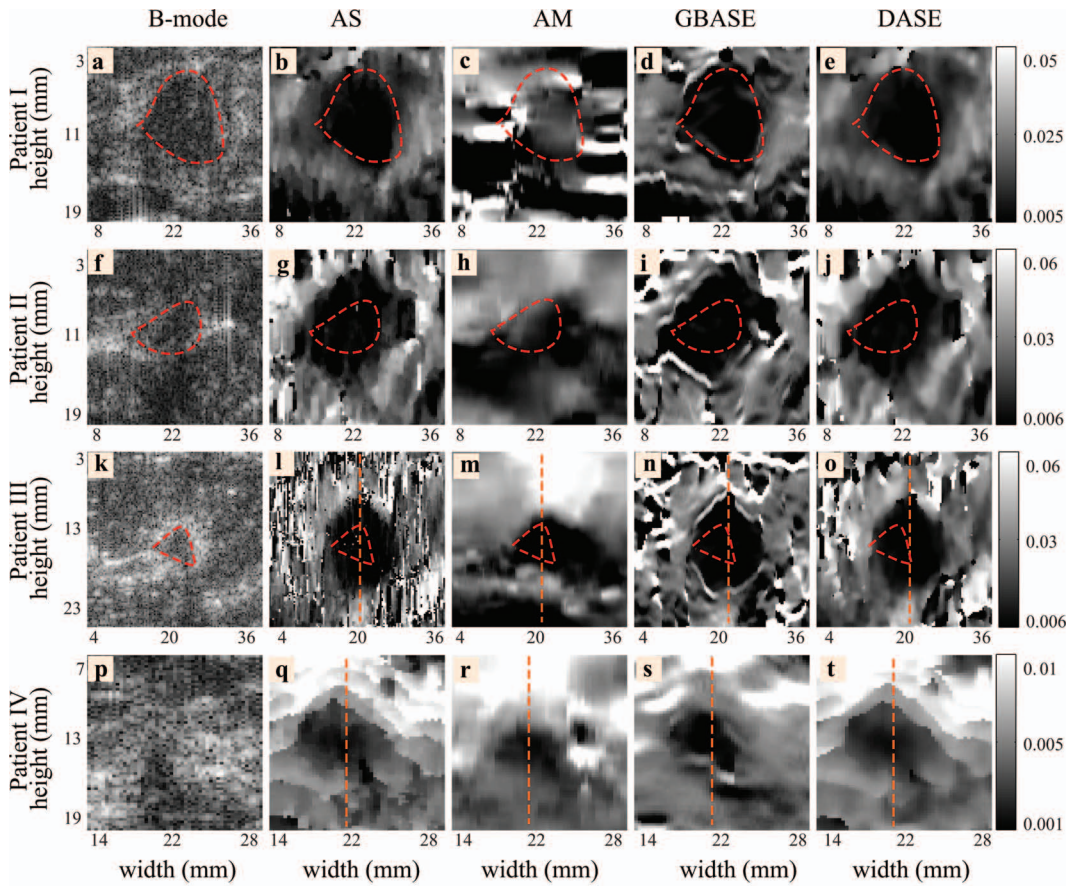

Fig. 13. Performance comparison of different methods using numerical performance metrics for the experimental phantom data. (a) SNRe vs. applied strain, (b) CNRe vs. applied strain.

Fig. 14. Strain images generated by different methods using *in vivo* breast ultrasound data. (a), (f), (k), (p) represent B-mode images of four patients. Results (b), (g), (l), (q) are produced by the AS method; (c), (h), (m), (r) are produced by the AM method; (d), (i), (n), (s) are produced by the proposed GBASE ($L_1 = 3$, $\chi_1 = 0.25$, $\nu = 0.5$); and (e), (j), (o), (t) are produced by the proposed DASE ($L_a = 3$, $L_1 = 3$, $\chi_a = \chi_1 = 0.25$, $\nu = 0.5$). The red dashed contours are drawn to compare the lesion sizes exposed in strain images with that of their corresponding B-mode images. For patient IV, the shape of the lesion is not understood. The size of the malignant objects in the strain images is larger than that in the corresponding B-mode images.

ever, that the AM method uses mex files but the others do not. By using mex files, the computational time performance of the proposed methods can also be improved.

IV. CONCLUSIONS

In this paper we have proposed two novel methods for the estimation of average displacement and strain in the time domain. We have shown that the average displacement and strain can be estimated by maximizing our proposed weighted cost function derived from the information of the neighboring windowed RF echoes. The effect of considering the lateral shift in the selection of 1-D RF pre- and post-compression segments has been also demonstrated for DASE as well as GBASE methods. Though the DASE method generally produces higher quality strain images, the GBASE technique is more computationally efficient. Moreover, the GBASE technique, unlike the conventional gradient based strain estimators, images the hard inclusions accurately. We also used a 2-D signal window to implement a 2-D DASE method. For the

2-D DASE method, we plotted the numerical performance metrics and saw that the 2-D DASE performs better than the DASE method though it has higher computational complexity. However, it has been shown by simulation and experimental results that the two proposed methods are more robust for a wide range of strain values than the compared techniques. We have shown strain profiles for the FEM phantom and calculated the overall MSE, which depict the superiority of our proposed methods over the other reported techniques. We also have plotted the strain profiles for very small and larger *in vivo* breast lesions where lesion dimensions estimated by our proposed methods matched well with those of the histology. Furthermore, only the proposed GBASE method successfully depicted the tiny lesion with the correct dimensions. The values of the quantitative performance metrics for the FEM and experimental phantom also indicate that the proposed methods generate higher quality and higher SNR strain images than the techniques that were compared in this paper. The salient feature of our technique is that, due to robustness to signal de-correlation, the stiff masses can be clearly viewed in the strain image and the lesion bound-
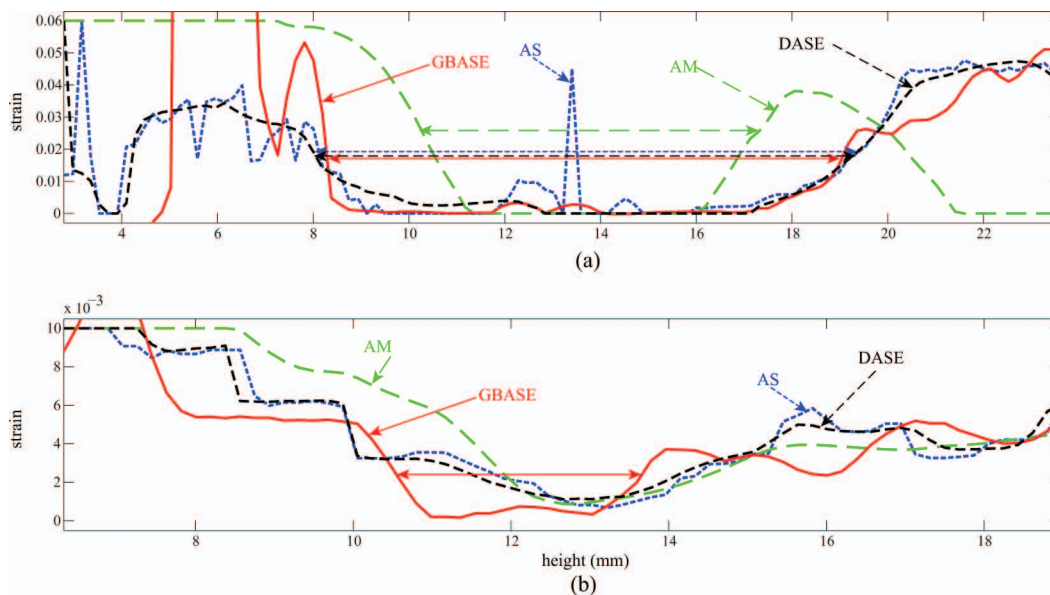
Fig. 15. Strain curves obtained for patients (a) III and (b) IV *in vivo* breast data by using different methods. Axial strain profile in an arbitrary scan line including the inclusion (as marked in Fig. 14). The estimated heights of the lesion of patient III for the AS, AM, GBASE, and DASE methods are 6.17, 11.26, 11.18, and 11.28 mm, respectively. The height of the lesion mentioned in the histology report is 11 mm. On the other hand, only the GBASE method shows a clear strain well for patient IV and the lesion height is found to be 3.07 mm (close to the histology report that reveals 3 mm).

ary can also be more clearly identified compared with the other methods.

References

[1] J. Ophir, "Elastography: A quantitative method for imaging the elasticity of biological tissue," *Ultrason. Imaging*, vol. 13, no. 2, pp. 111–134, 1991.

[2] J. Ophir, I. Cespedes, B. S. Garra, H. Ponnekanti, Y. Huanga, and N. Maklad, "Elastography: Ultrasonic imaging of tissue strain and elastic modulus in vivo," *Eur. J. Ultrasound*, vol. 3, no. 1, pp. 49–70, 1996.

[3] E. I. Céspedes, J. Ophir, H. Ponnekanti, and N. Maklad, "Elastography: Elasticity imaging using ultrasound with application to muscle and breast in vivo," *Ultrason. Imaging*, vol. 15, no. 2, pp. 73–88, 1993.

[4] J. Ophir, S. K. Alam, B. S. Garra, F. Kallel, E. E. Konofagou, T. Krouskop, C. R. B. Merritt, R. Righetti, R. Souchon, S. Srinivasan, and T. Varghese, "Elastography: Imaging the elastic properties of soft tissues with ultrasound," *J. Med. Ultrasound*, vol. 29, pp. 155–171, winter 2002.

[5] R. Zahiri-Azar and S. E. Salcudean, "Motion estimation in ultrasound images using time domain cross correlation with prior estimates," *IEEE Trans. Biomed. Eng.*, vol. 53, no. 10, pp. 1990–2000, 2006.

[6] S. K. Alam, "Novel spline-based approach for robust strain estimation in elastography," *Ultrason. Imaging*, vol. 32, no. 2, pp. 91–102, 2010.

[7] S. K. Alam, J. Ophir, and E. E. Konofagou, "An adaptive strain estimator for elastography," *IEEE Trans. Ultrason. Ferroelectr. Freq. Control*, vol. 45, no. 2, pp. 461–472, 1998.

[8] J. Ophir, S. K. Alam, B. S. Garra, F. Kallel, E. E. Konofagou, T. Krouskop, and T. Varghese, "Elastography: Ultrasonic estimation and imaging of the elastic properties of tissues,'' in *Proc. of the Institute of Mechanical Engineers*, Part H: *J. Eng. Medicine*, vol. 213, no. 3, 1999, pp. 203–233.

[9] T. Varghese, E. E. Konofagou, J. Ophir, S. K. Alam, and M. Bilgen, "Direct strain estimation in elastography using spectral cross-correlation," *Ultrasound Med. Biol.*, vol. 26, no. 9, pp. 1525–1537, 2000.

[10] S. K. Alam, F. L. Lizzi, T. Varghese, E. J. Feleppa, and S. Ramachandran, "Adaptive spectral strain estimators for elastography," *Ultrason. Imaging*, vol. 26, no. 3, pp. 131–149, 2004.

[11] U. Techavipoo and T. Varghese, "Wavelet denoising of displacement estimates in elastography," *Ultrasound Med. Biol.*, vol. 30, no. 4, pp. 477–491, 2004.

[12] S. K. Alam and J. Ophir, "Reduction of signal decorrelation from mechanical compression of tissues by temporal stretching-applications to elastography," *Ultrasound Med. Biol.*, vol. 23, no. 1, pp. 95–105, 1997.

[13] F. Kallel and J. Ophir, "A least-squares strain estimator for elastography," *Ultrason. Imaging*, vol. 19, no. 3, pp. 195–208, 1997.

[14] C. Pellot-Barakat, F. Frouin, M. F. Insana, and A. Herment, "Ultrasound elastography based on multiscale estimations of regularized displacement fields," *IEEE Trans. Med. Imaging*, vol. 23, no. 2, pp. 153–163, 2004.

[15] H. Rivaz, E. Boctor, P. Foroughi, R. Zellars, G. Fichtinger, and G. Hager, "Ultrasound elastography: A dynamic programming approach," *IEEE Trans. Med. Imaging*, vol. 27, no. 10, pp. 1373–1377, 2008.

[16] H. Rivaz, E. M. Boctor, M. A. Choti, and G. D. Hager, "Real-time regularized ultrasound elastography," *IEEE Trans. Med. Imaging*, vol. 30, no. 4, pp. 928–945, 2011.

[17] E. E. Konofagou, T. Varghese, J. Ophir, and S. K. Alam, "Power spectral strain estimators in elastography," *Ultrasound Med. Biol.*, vol. 25, no. 7, pp. 1115–1129, 1999.

[18] M. Bilgen and M. F. Insana, "Deformation models and correlation analysis in elastography," *J. Acoust. Soc. Am.*, vol. 99, no. 5, pp. 3212–3224, 1996.

[19] B. Pan, K. Qian, H. Xie, and A. Asundi, "Two-dimensional digital image correlation for in-plane displacement and strain measurement: A review," *Meas. Sci. Technol.*, vol. 20, no. 6, art. no. 062001, 2009.

[20] I. Céspedes and J. Ophir, "Reduction of image noise in elastography," *Ultrason. Imaging*, vol. 15, no. 2, pp. 89–102, 1993.

[21] T. Varghese and J. Ophir, "An analysis of elastographic contrast-to-noise ratio performance," *Ultrasound Med. Biol.*, vol. 24, no. 6, pp. 915–924, 1998.

[22] Z. Wang, A. C. Bovik, H. R. Sheikh, and E. P. Simoncelli, "Image quality assessment: From error visibility to structural similarity," *IEEE Trans. Image Process.*, vol. 13, no. 4, pp. 600–612, 2004.

[23] B. S. Garra, E. I. Céspedes, J. Ophir, S. R. Spratt, R. A. Zuurbier, C. M. Magnant, and M. F. Pennanen, "Elastography of breast lesions: Initial clinical results," *Radiology*, vol. 202, pp. 79–86, 1997.

Bangladesh, from 1986 to 1989. While pursuing graduate studies at the University of Rochester, his work on improving the ultrasonic estimation of blood velocity led to a patented technique for ultrasonic blood flow imaging. As a postdoctoral fellow at the University of Texas Medical School at Houston from 1995 to 1998, he worked on elastography, a new ultrasonic imaging modality to image elastic properties of tissue. Dr. Alam has been a Member of the Research Staff at Riverside Research Institute in New York since 1998, where he has been working on a variety of research topics involving biomedical imaging and signal processing. Since 2010, he has been a visiting faculty in the Department of Electrical and Electronic Engineering at Islamic University of Technology (IUT), Gazipur, Bangladesh. His research interests include diagnostic and therapeutic applications of ultrasound and optics, and signal/image processing with applications to medical imaging.

Dr. Alam has written over 30 papers in international journals and holds several patents. He is a member of Sigma Xi, Acoustical Society of America (ASA), Society of Photographic Instrumentation Engineers (SPIE), and a Senior Member of the American Institute of Ultrasound in Medicine (AIUM) and Institute of Electrical and Electronics Engineers (IEEE). Dr. Alam is also a member of the editorial board of the journal *Ultrasonic Imaging* and a recipient of the Fulbright Scholar Award in 2011–2012.

Mohammad Arafat Hussain was born in Magura, Bangladesh, in 1988. He received the B.Sc. degree in electrical and electronic engineering from Bangladesh University of Engineering & Technology (BUET), Dhaka, Bangladesh, in 2011.

He worked as a software engineer in Samsung Bangladesh R&D Center from March to June, 2011. He is currently a research engineer at DSP Research Lab, BUET, working on ultrasonic elasticity imaging and attenuation estimation. His research interests include ultrasonic imaging and tissue characterization.

Emran Mohammad Abu Anas was born in Dhaka, Bangladesh, in 1987. He received the B.Sc. and M.Sc. degrees in electrical and electronic engineering from Bangladesh University of Engineering & Technology (BUET), Dhaka, Bangladesh, in 2009 and 2011, respectively.

In 2009, he joined BUET as a Lecturer in the Department of Electrical and Electronic Engineering. His research interests include CT and ultrasonic imaging.
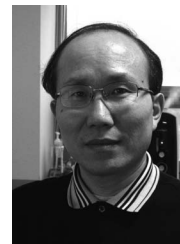
Sheikh Kaisar Alam was born in Bangladesh. He received the Bachelor of Technology (Honors) in Electronics and Electrical Communication Engineering from the Indian Institute of Technology, Kharagpur, India in 1986, and the M.S. and Ph.D. degrees in Electrical Engineering from the University of Rochester, Rochester, NY, in 1991 and 1996, respectively.

Dr. Alam was a lecturer in the Department of Electrical and Electronic Engineering at the Bangladesh Institute of Technology, Rajshahi,

Soo Yeol Lee received the M.S. and Ph.D. degrees in electronic engineering from the Korea Advanced Institute of Science and Technology (KAIST), Seoul, South Korea, in 1985 and 1989, respectively. He was with Department of Biomedical Engineering in Konkuk University, South Korea, from 1992 to 1999. In 1999, he joined the Department of Biomedical Engineering in Kyung Hee University, South Korea, where he is the director of the functional and metabolic imaging research center (FMIC). His research interests are MRI, CT, elastography, and medical image processing.

Md. Kamrul Hasan received the B.Sc. and M. Sc. degrees in electrical and electronic engineering from Bangladesh University of Engineering and Technology (BUET), Dhaka, Bangladesh, in 1989 and 1991, respectively. He received his M.Eng. and Ph.D. degrees in information and computer sciences from Chiba University, Japan, in 1995 and 1997, respectively.

In 1989, he joined BUET as a Lecturer in the Department of Electrical and Electronic Engineering. He is presently working as a Professor in the same department. He was a post-doctoral fellow and research associate at Chiba University, Japan, and Imperial College, London, respectively. He worked as a short-term invited research fellow at the University of Tokyo, Japan, and Professor of International Scholar of Kyung Hee University, Korea. His current research interests are in digital signal processing, adaptive filtering, speech and image processing, and medical imaging. He has authored more than 100 scientific publications.

Prof. Hasan is a member of the editorial board of Conference Papers in Signal Processing, Hindawi Publishing Corporation, and a senior member of IEEE.